HOKKAIDO UNIVERSITY

Title	Characteristics of glacier surface weathering crust and light-absorbing particles, and their combined impact on glacier albedo at the Potanin Glacier, Mongolia
Author(s)	Sakai, Akiko; Kobayashi, Kino; Ono, Masato et al.
Citation	The Cryosphere, 20(9), 5181-5198 https://doi.org/10.5194/tc-20-5181-2026
Issue Date	2026-09-16
Doc URL	https://hdl.handle.net/2115/100428
Rights(URL)	https://creativecommons.org/licenses/by/4.0/
Type	journal article
File Information	tc-20-5181-2026.pdf

Hokkaido University Collection of Scholarly and Academic Papers : HUSCAP

The Cryosphere, 20, 5181–5198, 2026
https://doi.org/10.5194/tc-20-5181-2026
© Author(s) 2026. This work is distributed under
the Creative Commons Attribution 4.0 License.

The Cryosphere
Open Access
EGU

Characteristics of glacier surface weathering crust and light-absorbing particles, and their combined impact on glacier albedo at the Potanin Glacier, Mongolia

Akiko Sakai[1], Kino Kobayashi[2,a], Masato Ono[3,b], Sayako Ueda[1], Sho Ohata[4,c], Akira Watanabe[5], Kazuo Osada[1], Nozomu Takeuchi[6], Prevdagva Khalzan[7], Sumito Matoba[8], Tomonori Tanikawa[9], and Teruo Aoki[9]

[1]Graduate School of Environmental Studies, Nagoya University, Nagoya, Japan
[2]Graduate School of Science and Engineering, Chiba University, Chiba, Japan
[3]Center for Ecological Research, Kyoto University, Otsu, Shiga, Japan
[4]Institute for Space–Earth Environmental Research, Nagoya University, Nagoya, Japan
[5]Graduate School of Bioagricultural Sciences, Nagoya University, Nagoya, Japan
[6]Center for Environmental Remote Sensing, Chiba University, Chiba, Japan
[7]Information and Research Institute of Meteorology, Hydrology and Environment, Ulaanbaatar, Mongolia
[8]Institute of Low Temperature Science, Hokkaido University, Sapporo, Japan
[9]Meteorological Research Institute, Japan Meteorological Agency, Tsukuba, Ibaraki, Japan
[a]now at: Arctic Environment Research Center, National Institute of Polar Research, Tachikawa, Japan
[b]now at: Graduate School of Arts and Sciences, University of Tokyo, Meguro, Japan
[c]now at: Graduate School of Environmental Studies, Nagoya University, Nagoya, Japan

Correspondence: Akiko Sakai (shakai@nagoya-u.jp)

Received: 3 February 2026 – Discussion started: 11 March 2026
Revised: 15 July 2026 – Accepted: 4 September 2026 – Published: 16 September 2026

Abstract. The glacier ablation areas in the mid-latitude mountains have a dark surface due to abundant light-absorbing particles (LAPs) (mineral dust, organic matter of microbial origin, black carbon). Conversely, the development of weathering crust on the bare ice surface increases the surface albedo. During the summers of 2022 to 2024, field observations were conducted on the Potanin Glacier in Mongolia. In this study, we defined the low-density surface layer within the weathering crust as the weathering granular ice layer. Here, we clarify the relationship between broad-band albedo (BB albedo), the thickness of surface granular ice, and LAP content within the granular ice layer. In situ measurements of BB albedo showed a significant positive correlation with the thickness of the granular ice layer (log10-transformed; $r = 0.41$, $p < 0.001$), and a relatively strong negative correlation with organic matter (log10-transformed; $r = -0.75$, $p < 0.001$). It was also revealed that higher concentrations of LAPs inhibited the thickening of the weathering crust layer. Furthermore, the observed variability in correlation strength across different particle concentrations, together with evidence from previous studies, suggests that mineral particles, whether exposed within the glacier or deposited onto the glacier surface from the atmosphere, support the growth of microorganisms living on the ice. The subsequent proliferation of these microorganisms and the production of humic-like substances are considered to increase surface adhesiveness, thereby facilitating the adsorption of black carbon.

1 Introduction

Mountain glaciers have been shrinking in recent years due to global warming (Hugonnet et al., 2021; The GlaMBIE Team, 2025). Accurately projecting the mass balance of glaciers is therefore crucial. Net shortwave radiation is the primary heat source for glacier melting in most cases (e.g., Braithwaite, 1995; Greuell and Smeets, 2001; Pellicciotti et al., 2005).

The albedo is crucial to this melting process because it determines the fraction of downward shortwave radiation reflected, which, in turn, affects the incoming shortwave radiation. Clean snow and ice have relatively high albedos. However, LAPs such as mineral dust, black carbon, and microorganisms significantly reduce albedo, thereby substantially increasing the absorption of shortwave radiation. Recent studies in Europe have revealed a significant correlation between the minimum summer albedo values of individual glaciers and their annual mass balance (Di Mauro and Fugazza, 2022).

Important factors that determine the albedo of a snow surface are the size of the snow particles, snow grain shape, snowpack thickness, snow microstructure, snowpack density and the concentration of light-absorbing particles (LAPs) – substances such as mineral dust and black carbon that reduce how much light is reflected (e.g., Warren, 1982; Aoki et al., 2003; Flanner and Zender, 2006; Painter et al., 2001). Albedo reduction due to LAPs has been documented in previous studies (e.g., Warren and Wiscombe, 1980; Flanner et al., 2007; Dumont et al., 2017; Skiles and Painter, 2017). Physically based snow albedo models that account for radiative transfer processes within the snow layer have been developed by several researchers: SNICAR (Flanner et al., 2021), PBSAM (Aoki et al., 2011), and TARTES (Picard and Libois, 2024). Recently, biological particles (such as algae that grow on snow) that also affect albedo reduction have been studied (Cook et al., 2017b; Onuma et al., 2020; Halbach et al., 2022). Cook et al. (2017a) included biological particles in radiative transfer models. The authors presented a new model, "BioSNICAR", which combines cell-specific optical properties with radiative transfer theory to quantify biological albedo reduction. Using this model, they simulated how cell size and pigment composition influence reflectance spectra and established a method to isolate biological effects from the intrinsic properties of ice and inorganic particles (e.g., dust and black carbon). Then, they demonstrated that biological particles significantly contribute to albedo reduction.

However, albedo's effect on glacier melting is especially important in ablation areas, where the "ice" surface is exposed. Surface albedo here strongly impacts glacier mass balance (Naegeli and Huss, 2017). Observations of albedo in ablation areas are limited. Hartl et al. (2020) summarised bare-ice albedo observations on glaciers. They measured spectral reflectance (HCRF, spherical–conical reflectance factors) of bare ice. They classified ice as wet or dry, non-debris or debris, then compared these types with LANDSAT imagery. Whicker et al. (2022) developed a spectral albedo model for glacier ice, SNICAR-ADv4, which includes LAP. They recommended setting a thin layer of snow over bare ice.

Furthermore, in the ablation zone where ice surfaces are exposed, penetration of solar radiation into the ice induces subsurface melting, leading to the formation of a porous, mechanically fragile weathering crust. Weathering crust and LAP are important factors changing albedo in glacier ablation areas (Tedstone et al., 2020). Weathering crust observations were conducted in Greenland (Cook et al., 2016; Irvine-Fynn et al., 2021), Alaska (Christner et al., 2018) and East Antarctica (Traversa and Di Mauro, 2024). Woods and Hewitt (2023) modelled weathering crust based on microbial activity and chemical composition, assuming it exists in Greenland. They found that shortwave (surface-penetrating) radiation is significant for weathering crust structure.

In High Mountain Asia, glaciers have heavier abundances of mineral dust, black carbon, and microorganisms on their surfaces than glaciers in Patagonia, Alaska, and the Arctic regions (Takeuchi et al., 2005; Takeuchi et al., 2008). These light-absorbing particles are therefore expected to have a strong impact on reducing ice albedo. In addition, the development of a weathering crust quantitatively increases surface albedo. However, to date, only Takeuchi et al. (2005) have investigated weathering crust on glaciers in High Mountain Asia. Granular ice has been observed by Zhang et al. (2017) and Li et al. (2017). It has been reported that granular ice contains as many particles (mineral dust and black carbon) as old snow. These particles contribute to albedo reduction. While the role of LAPs in albedo reduction is well studied, there has been no research in High Mountain Asia explicitly investigating how weathering crust and surface granular ice relate to particles and affect albedo.

In this study, we focused not only on LAPs but also on weathering crust, especially the granular ice in the surface layer. We performed investigations and analyses to clarify the relationships between albedo and these elements. We targeted mineral dust (MD), black carbon (BC), and organic matter (OM) as the three major LAPs. The aim of this study is to elucidate the interrelationships among light-absorbing particles (LAPs) and between surface granular ice and LAPs in the High Mountain Asia (HMA), and to clarify the differing roles of each LAP in glacier surface albedo reduction and in influencing the development of the weathering crust.

2 Observation

2.1 Study area and previous study

We conducted field observations at the Potanin Glacier (87.866° E, 49.154° N), which is located in the northern part of the HMA, on the western edge of Mongolia (Fig. 1a). In this region, glaciers are classified as summer accumulation type, and about 80 % of annual precipitation falls in summer (Khalzan et al., 2022). In Mongolia, research has been conducted on observations and modelling of glacier mass balance (Khalzan et al., 2022) and runoff (Pan et al., 2019; Khalzan et al., 2025), as well as glacier area changes (Pan et al., 2017). Khalzan et al. (2025) reported that glacier meltwater accounted for 28 % of river runoff even though the glacier area ratio was only 0.8 % in the upper Ulgii basin, includ-

ing the Potanin Glacier, from 2000 to 2020. The large runoff from glaciers would be due to recent glacier shrinkage.

The Potanin Glacier in the Tavan Bogd region reaches a maximum elevation of 4374 m a.s.l. (Mt. Khuiten). Its terminus sits at 2907 m a.s.l. The glacier is 10.4 km long and covers 24.7 km^2, making it the largest in Mongolia. Mass balance data have been collected since 2003 (Khalzan et al., 2022). The estimated glacier-wide mass balance at the Potanin Glacier is -158 ± 258 mm w.e. yr^{-1} from 1980 to 2018, using optimised precipitation data (Khalzan et al., 2022).

2.2 Observation and sample analysis

Field observations were conducted during the ablation season in July–August 2022, 2023, and 2024. The sampling periods varied each year: 3 to 11 July 2022, 4 July to 8 August 2023, and 22 July to 2 August 2024. The observation items are summarized in Table 1.

2.2.1 Shallow ice cores for ice density profile at depth

We took two shallow ice cores at ST2c and ST3c (Fig. 1b) in July 2023 using an ice auger (Olympia Kogyo Co., Ltd.) to obtain an ice density-depth profile, including the weathering crust. For each separated ice core, we measured the weight, length, and cross-sectional diameter at the drilling site using a caliper. We also measured the thickness of the weathering crust at the same sites.

2.2.2 LAPs, surface granular ice thickness and BB albedo

At the Potanin Glacier, the uppermost part of the weathering crust features a layer with particularly low ice density, characterised by a granular ice texture. The boundary between this layer and the underlying high-density crust layer can be easily identified and is referred to in this study as the surface granular ice layer. The thickness of the surface granular ice layer was used as an indicator of the degree of weathering crust development (see Sect. 3.1 for observation results). This layer contains exceptionally high concentrations of light-absorbing particles (LAPs). It can be regarded as corresponding to the dirt surface layer (Ueda et al., 2026b).

We performed the following measurements and sampling to investigate the relationships among broadband albedo (BB albedo), the three major LAPs (MD: Mineral dust, OM: Organic matter, BC: Black carbon), and granular ice thickness (GIT) of the weathering crust. BB albedo is defined as the surface albedo integrated over a certain wavelength range. Here, we define BB albedo as the fraction of the total incoming solar radiation reflected by a surface over the entire shortwave spectral range.

There are five stakes (ST1c, ST2c, ST3c, ST4c, ST5r) along the central line of the ablation area (Fig. 1b), from which we collected particles on the glacier surface. At two to ten sites near each stake, we measured broadband (BB) albedo and collected particle samples, avoiding snow surfaces. Debris from the nunatak accumulates and forms dark longitudinal stripes in the ablation area (Fig. 1b). Numerous transverse dark bands with exposed mineral dust, mainly upstream of ST2c, were also observed. Both dark and clean surfaces were therefore found around each stake. In 2022, we did not distinguish between dark and clean surfaces during sampling; however, in 2023 and 2024, we sampled both types for BB albedo measurement and particle collection. BB albedo was measured five times at each site using paired pyranometers (CMP-3, Prede Co., Ltd., wavelength region: $\lambda = 300$–2800 nm) oriented both upward and downward, parallel to the glacier surface and level with the sky. The average and standard deviation were calculated to obtain representative annual BB albedo values for each stake. The standard deviation was used as the uncertainty of BB albedo. Albedo measurements were carried out between 11:00 and 15:30 local time (LT), during which the solar zenith angle ranged from 26 to 45°. During the albedo measurements, the height of the radiometer was about 20 $(= a)$ cm above the ice surface. The paired pyranometers receive shortwave radiation from the glacier surface hemisphere and the atmospheric hemisphere. Since the observation targets a uniform circle with a radius of 50 $(= b)$ cm as much as possible, when the projected solid angle is considered geometrically, $b^2/(a^2 + b^2)$, the target circle occupies approximately 0.86 of the projected solid angles of the hemisphere.

After measuring the BB albedo, we collected particle samples using a stainless-steel scoop. Samples for OM and MD measurements, including the entire surface granular ice layer with particles, were placed in a plastic bag. After collecting the samples, we measured the area of the sampled square (length and width) and the sampling depth (i.e., the thickness of the granular ice) at four points along the sides of the sampling square. The plastic bag containing the samples was brought to base camp, where the ice was melted over the course of 1 d, leaving the deposited particles. All deposited particles were then transferred to 30 mL plastic bottles containing 1 % formalin.

In the laboratory, the samples were dried in pre-weighed crucibles at 60 °C for 1–2 d. The dry weight of particles (MD and OM) were then measured. To remove OM, dried samples were combusted at 500 °C for 3 h in an electric furnace. These methods were based on Takeuchi and Li (2008), as modified from Dean (1974). Finally, MD and OM amounts per area were calculated using the sampling area.

The amount of OM was calculated by burning the sample in an oven at 500 °C and measuring the weight difference before and after burning. BC is difficult to burn at 500 °C (Leifeld, 2007), so it is highly likely that it was measured as part of the mineral mass (i.e., MD contains BC), but the amount of BC measured using a different sample from the same location is four orders of magnitude smaller than that of MD (Sect. 3.2 and 3.3), so the effect can be ignored.

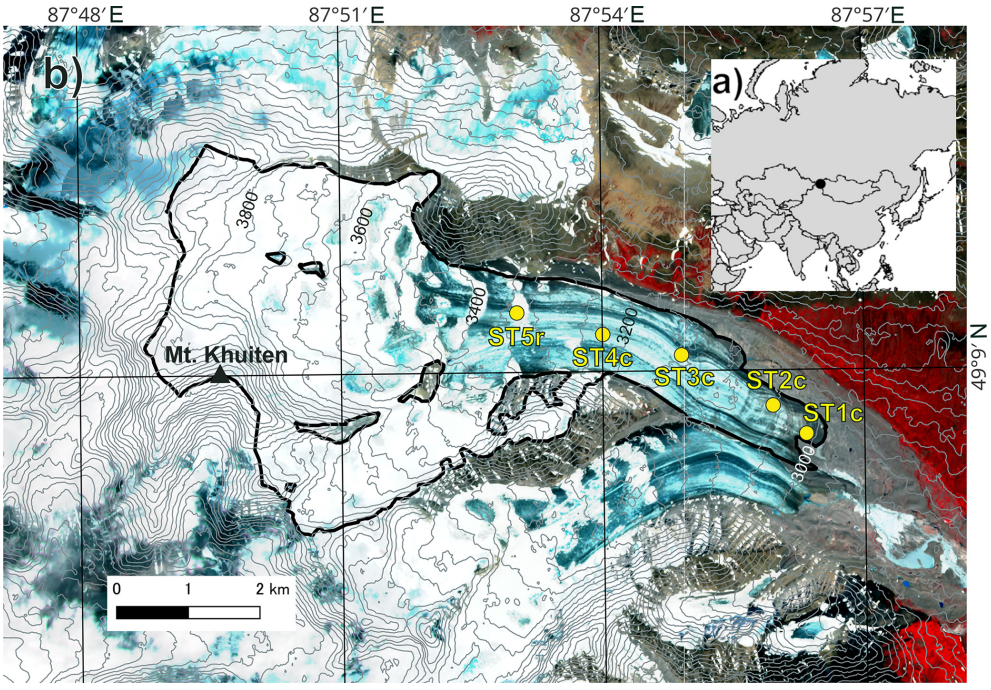


Figure 1. Location map of the Potanin Glacier **(a)** and observed stake location at the Potanin Glacier **(b)**. The edges of the Potanin glacier are outlined in black. Contour lines are drawn at 50 m intervals. Yellow numbers indicate the location of stake, sampling site. The back satellite imagery is Sentinel 2 (False color) acquired on 15 July 2023.

Table 1. Summary of observation items, locations, observation periods, and sample quantities. BB albedo: broadband albedo; MD: mineral dust; BC: black carbon; OM: organic matter. Parentheses indicate the year of acquisition.

Observation item	Location	Year	Date/period	Time/interval	Sample quantity
BB albedo	ST1c–ST5r, 2–10 sites around each stake	2022–2024	3–11 Jul (2022); 4 Jul–8 Aug (2023); 22 Jul–2 Aug (2024)	11:00–15:30 LT;	39(2022), 44(2023), 42(2024) sites 5 measurements/site
MD and OM	Same sites as BB albedo	2022–2024	Same as above	After BB albedo measurement	39(2022), 44(2023), 42(2024) samples
BC	Same sites as BB albedo	2024	22 Jul– 2 Aug	After BB albedo measurement	41 samples
Ice density profile (Shallow ice cores)	ST2c, ST3c	2023	July	–	2 cores (one core/site)
Ice temperature	ST2c, ST5r	2023	Jun–Aug	Every 15 min	–
Spectral albedo	ST2c, dark and clean surfaces	2024	24 Jul	–	5 measurements/condition
Ablation	ST1–ST5 stake network	2022–2024	Melt season	∼ 5 d interval	3 stakes/site (ST1c–ST4c); 2 at ST5r
Humic/fulvic acids	Ablation area	2022 and 2023	Jul–Aug	–	< 53 and 53–150 µm fractions
X-ray diffraction (XRD)	ST1c–ST5r	2022	July	–	One sample /stake

For MD and OM, there is some uncertainty associated with the mass measurements themselves; however, it is considered negligible compared to the uncertainty arising from estimating the sampling area. Sampling was conducted over an area of approximately 150×150 mm on the ice surface. Assuming an uncertainty of ± 2.5 mm in each side length, the sampled area ranges from 21,025 $(145 \times 145)\,\mathrm{mm}^2$ to 24 025 $(155 \times 155)\,\mathrm{mm}^2$, resulting in an uncertainty of approximately ± 7.0 % in the mass per unit area.

Samples for BC analysis were collected only in 2024. BC measurement results were detailed in Ueda et al. (2026b). After measuring the BB albedo, we also collected surface granular ice samples for BC analysis. We collected 41 BC samples in 2024. We used a stainless steel shovel to scoop all layers of granular ice from a square area about 10 cm on each side and placed them in an additive-free low-density polyethene bag. This material generates almost no particles. Once melted, each sample was thoroughly stirred and immediately transferred to 30 or 50 mL glass bottles (SV30 and SV50; Nichiden Rika Glass Co., Ltd.). During transport and storage, samples were kept refrigerated and unfrozen to prevent BC loss from refreezing. Details of the measurement system used in this study and the evaluation results of the sample storage method for BC measurements were reported by Ueda et al. (2026a). In the laboratory, we attempted to measure BC concentration using a system consisting of a pneumatic nebulizer (Marin-5; Cetac Technologies Inc., USA) and a single-particle soot photometer (SP2: Droplet Measurement Technologies (DMT), Longmont, CO, USA) (Mori et al., 2016; Sinha et al., 2018). A standard SP2 measures the mass of each BC particle with mass equivalent diameter (DBC) within the 70–850 nm range by assuming a BC particle density of $1.8\,\mathrm{g\,cm}^{-3}$ (Moteki et al., 2010), whereas the SP2 used for this study measures masses of BC particles within the 70–3000 nm range by expanding the upper limit of the detected incandescence signal in the standard SP2 (Mori et al., 2016). BC mass concentration was obtained by integrating the mass of BC particles. The particle sample in surface granular ice contains a significant amount of non-BC material, including MD and OM. Before measurement using the nebulizer-SP2 system, liquid samples in glass vials were sonicated for 10 min to minimize the loss of BC particles attached to the other LAP and the vial wall. To prevent clogging of the nebulizer-SP2 system, after settling of large dust particles by standing for 10 min after sonication for all samples, suspended liquid samples in vial middles were dispensed into 10 ml PET vials (JST-R/N10; Nikko Hansen & Co., Ltd.), and then measured using the nebulizer-SP2 system. At dispensing, samples were diluted 3–10 times with Milli-Q water based on turbidity. The nebulizer-SP2 system measures the mass of BC per volume of water. During MD measurements at the same site, we measured ice density and sampling area, which were used to calculate BC per area. Regarding the uncertainty of the BC amount per unit area, the sampling area is the dominant source of uncertainty in this conversion. Therefore, the uncertainty is estimated at ± 7.0 % for MD and OM.

2.2.3 Ablation rate of the glacier and ice temperature profile at the surface layer

Glacier surface decline was observed using stakes at approximately 5 d intervals during the melt season from 2022 to 2024. Details of the stake measurements are provided in Khalzan et al. (2022), and stake locations are shown in Fig. 1b of Khalzan et al. (2022). The surface decline was converted to mass balance, assuming an ice surface density of $900\,\mathrm{kg\,m}^{-3}$. Because snow accumulation on the glacier was limited, negative mass balance was considered equivalent to ablation. Daily mean values were calculated for each observation interval. These values were then used to determine the mean velocity over the sampling period. At sites ST1c–ST4c, three stakes (centre, R, and L) were installed at the same elevation in the transverse direction. At ST5c, two stakes (R and L) were installed. To estimate representative daily ablation at each elevation, the mean of the stakes at that elevation was used. If the errors in scale reading and surface roughness are assumed to be 10 mm, the ablation measurement error is $20\,\mathrm{mm} \times 900\,\mathrm{kg\,m}^{-3} / 1000\,\mathrm{kg\,m}^{-3} / 5\,\mathrm{d}, = 3.6\,\mathrm{mm\ w.e.\ d}^{-1}$, taking into account that the measurements were conducted every 5 d.

Ice temperatures up to 1 or 2 m in depth were measured at ST2c and ST5r in 2023. The sensor was set at depths of 1, 0.5, or 0.2 m or at 2 or 1 m. The measurement interval was 15 min. Measurements were conducted using a HOBO data logger (model: MX1105). This logger was equipped with an SD-TEMP sensor with an accuracy of ± 0.15 °C. Changes in sensor depth associated with surface melting are discussed in Sect. 3.1.

2.2.4 Spectral albedo of the weathering crust

Spectral albedo of the glacier surface was measured with a spectrometer system on 24 July 2024. The spectrometer system consists of two spectrometer devices for different spectral domains of $\lambda = 350$–1100 nm (Ocean-HDX, Ocean Insight, Inc.) and $\lambda = 900$–1600 nm (NIRQuest+1.7, Ocean Insight, Inc.). The spectral albedo is the spectral fraction of the reflected component of the surface to the downward radiant flux density. To measure these flux densities accurately, we used a device using a white reflectance standard (WRS, Spectralon, Labsphere Inc.) and a rotating mount for directing the optical fiber from the spectrometers to WRS, following the setup described in Aoki et al. (2000). The WRS was positioned parallel to the glacier surface. To ensure measurement accuracy, calibration was performed to correct for a fraction of the field of view seen from the WRS obstructed by an optical fiber arm and to verify the cosine property (the ability of the WRS to reflect light isotropically, following the cosine law) of the WRS, as in Aoki et al. (2000).

All measurements were conducted in a unified sequence. Five repeated measurements, alternating between upward and downward, were taken, and the five albedos were averaged for each surface condition. We identified two surface types in the area around ST2c: dark and clean surfaces. Spectral albedo was measured for both the weathering crust surface and after granular ice removal (which covered approximately 2 m^2). The WRS height above the glacier surface was measured at 40 cm. After spectral albedo measurements, we performed particle sampling with quadrats, including the granular ice layer. Granular ice thickness was measured at four quadrangle sides. For all samples, granular ice was loosened, placed on black felt, photographed, and the diameter of ice grains was measured with ImageJ (https://imagej.net/ij/, last access: 1 July 2026). LAPs (light-absorbing particles: MD, OM, and BC) were analysed by the same method as in the previous section. Spectral albedo measurements were also performed for the bubble-rich ice underlying the granular ice layer, but particle sampling was not carried out for this layer.

2.2.5 Analysis of humic substances

Humic substances, complex mixtures of partially decomposed OM, were extracted from the LAP samples using the NAGOYA method (Kuwatsuka et al., 1992; Ikeya and Watanabe, 2003). Briefly, humic and fulvic acids were extracted with 0.1 M NaOH at a rate of 300 mL g^{-1} soil carbon (5 mL g^{-1} for 2023 samples due to low carbon content) by shaking for 24 h at 25 °C under a N_2 atmosphere. The extract was acidified to pH 1.5 with 3 M H_2SO_4, allowed to stand overnight, and centrifuged to separate humic acids (precipitate) from the supernatant, which included fulvic acids (fulvic fraction). The fulvic fraction was applied to the column packed with Supelite DAX-8 (Supelco, Bellefonte, PA, USA) to which fulvic acids are adsorbed, and the amount of fulvic acids on a carbon basis was obtained by subtracting the amount of carbon in the eluate from that in the fulvic fraction applied to the column. For blank correction, 0.05 M H_2SO_4 was used instead of the sample solution. Organic carbon concentration in the solution sample was measured using a total organic carbon analyzer (TOC-VCPH, Shimadzu) after purging with N_2 to remove CO_2. The precipitated humic acids were re-dissolved in 0.1 M NaOH, and the absorbance at 600 nm (A_{600}) and 400 nm (A_{400}) was immediately measured using a spectrophotometer (UV-2450, Shimadzu). A portion of each fraction was diluted 5-fold with 0.067 M KH_2PO_4, and the organic carbon concentration was determined. The degree of humification of humic acids was evaluated using two variables: A_{600}/C and $\log(A_{400}/A_{600})$, where C is the organic carbon concentration (mg mL^{-1}). Humic acids were classified into four types: A, B, P, and Rp according to $\log(A_{400}/A_{600})$–A_{600}/C diagram (Ikeya and Watanabe, 2003). The reproducibility of this determination method for humic fractions, based on the coefficient of variation (CV; $n = 5$), is < 6 %, while the CVs for $\log(A_{400}/A_{600})$ and A_{600}/C are 0.2 % and 2.5 %, respectively (Watanabe et al., 2007).

2.2.6 X-ray diffraction analysis of particles

X-ray diffraction analysis (XRD) was conducted to investigate the mineralogical composition of the particle samples on the glacier surface. Samples were collected from each stake with a steel scoop and placed in polyethene bottles. The samples were then dried at 60 °C, powdered, and analyzed by XRD using a Rigaku Ultima IV diffractometer at Chiba University, Japan. The X-ray target was CuK α (copper K alpha radiation), tube voltage 40 kV, and tube current 25 mA. Scans were performed from 4 to 60° (2θ), where 2θ represents the angle between the incident and diffracted X-rays, at a rate of 2° min^{-1} (2θ) (Nagatsuka et al., 2014).

3 Results and Discussion

3.1 Profile of ice temperature and ice density at the shallow layer

Surface melting causes surface lowering, which changes the depths of ice temperature sensors. Based on surface-lowering rate data collected about every 5 d, we assumed a constant rate between measurements. Using this, we calculated the daily positions of ice temperature sensors. For scatter plots of depth versus temperature (Fig. 2), we used the ice temperature readings at local noon. Figure 2 shows temperate ice reaching 0.35 m at ST2c and 0.60 m at ST5r by midsummer 2023. The temperate layer at ST5r is thicker than at the lower-elevation ST2c, likely because ST2c has thinner winter snow cover. As a result, information on low winter temperatures was stored at ST2c, while thicker snow at ST5r provides more insulation, reducing glacier cooling at ST5r compared to ST2c.

Weathering crust forms when solar radiation penetrates the ice and is absorbed, causing internal melting at 0 °C (Christner et al., 2018; Woods and Hewitt, 2023). Then, the weathering crust can be considered equivalent to temperate ice.

These results differ from previous studies, which found that the weathering crust (the upper porous layer of melting ice) develops to depths greater than 1 m in Greenland (Cooper et al., 2018) and 2 m in Alaska (Christner et al., 2018). In contrast, on the Potanin Glacier, the weathering crust was much thinner, with a maximum thickness of only 0.6 m.

Density profiles of ice were obtained for ST2c and ST3c (Fig. 3). The surface layer is 20 mm thick for ST2c and 100 mm for ST3c, with a density of 300–500 kg m^{-3}. Below this low-density surface, the density rises to 700–850 kg m^{-3}, close to the typical solid ice density of about 917 kg m^{-3}. The profile shows abrupt changes with depth; ice density increases above 700 kg m^{-3}, and the boundary

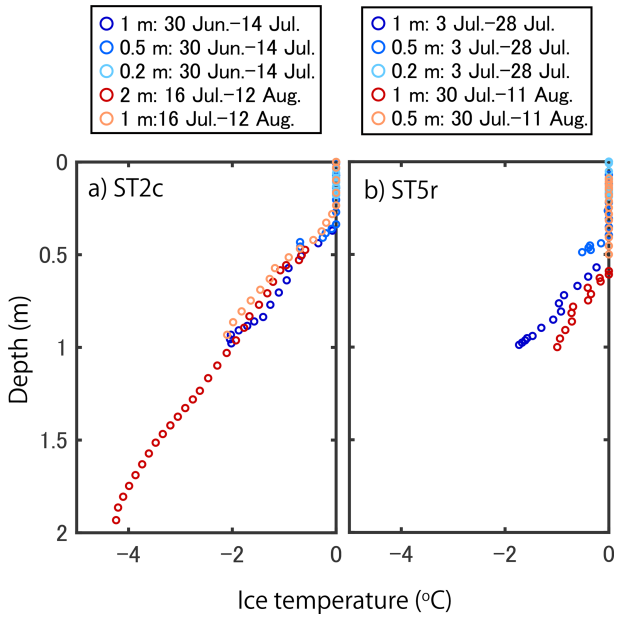


Figure 2. Daily ice temperature profiles at ST2c **(a)** and ST5r **(b)** in 2023. Sensor depths were corrected using surface decline data obtained from stake observations. Each legend shows the first setting depths of the ice temperature sensor, and the measurement date.

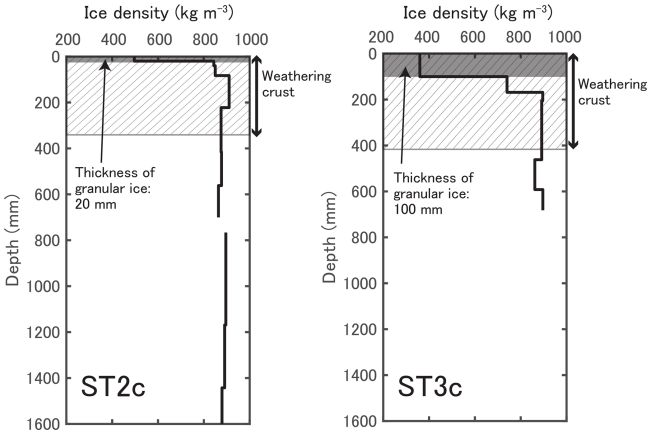


Figure 3. Ice density profile at ST2c (left) and at ST3c (right) at the surface layer. The grey areas indicate layers of weathering granular ice. The weathering crust thickness estimated from ice temperature is indicated by the hatched area.

is clearly identified using a scoop. The surface granular ice layer consists of either individual particles or fragile, porous granular ice, i.e., loosely packed grains with many air gaps (Supplement Fig. S1a, b). In contrast, the underlying weathering crust contains many air bubbles and is mostly closed off (Fig. S1c). In this study, we refer to this type of ice as "bubble-rich ice", as shown in Figs. 3 and 4.

Furthermore, ice core observations indicate that within approximately 30–50 cm below the surface, the ice appears white and turbid due to air bubbles, representing a weathering crust – that is, a 0 °C layer where melting occurs. The surface layer is characterized by strong transmission and absorption of solar radiation, as well as a high concentration of particles. As a result, melting between ice grains is enhanced, leading to the formation of granular ice. In contrast, the underlying bubble-rich ice exhibits lower transmission and absorption of solar radiation than the surface layer, and because the air bubbles are not interconnected, particles cannot penetrate into this layer. Consequently, it has not yet transformed into granular ice. However, with further absorption of solar radiation, the bubbles may begin to interconnect, allowing particles to infiltrate, which would in turn enhance solar absorption.

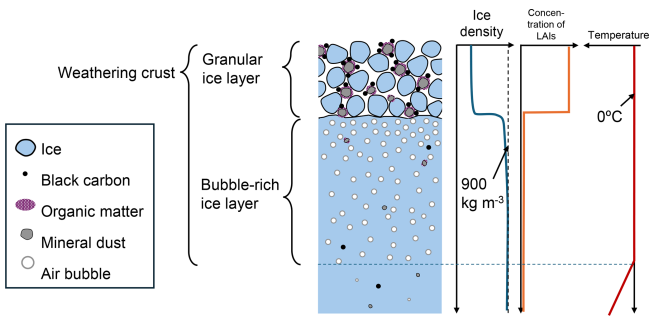


Figure 4. Conceptual diagram of weathering crust structure: granular ice layer and bubble-rich ice layer underlying the granular ice layer. High content of mineral dust covered with OM and BC in the granular ice layer. And a high content of air bubbles and less particles in the bubble-rich ice layer. Conceptual depth profiles of ice density, LAP content, and ice temperature based on observed data.

Because weathering crust development increases albedo (Tedstone et al., 2020), this study uses the thickness of the low-density granular ice layer (a loosely packed, porous surface ice formed from melting and refreezing) at the top of the weathering crust as a physical parameter to compare albedo and weathering crust development.

3.2 Altitudinal distribution of BB albedo, granular ice thickness and particles

Figure 5 shows the mean and standard deviation of MD, OM, BC, and GIT ABL for each stake and year from 2022 to 2024. Sampling at ST1c was not conducted in 2023 or 2024. Analysis of OM from the clean area at ST4c in 2023 was not conducted. The Potanin Glacier surface clearly contrasts particle-rich and particle-poor areas; This contrast is likely governed by the distribution of medial moraines and by mineral exposure resulting from ice melt. In clean areas with fewer particles, higher BB albedo reduces melting and creates elevated features. Thus, dark and clean surfaces are easily distinguished in the field.

The averages of BB albedo, GIT, MD, and OM % (organic matter ratio) from 2022 to 2024 were 0.33 ± 0.019 (range: 0.15–0.64), 28.6 ± 2.1 mm (range: 3.9–95.0 mm),

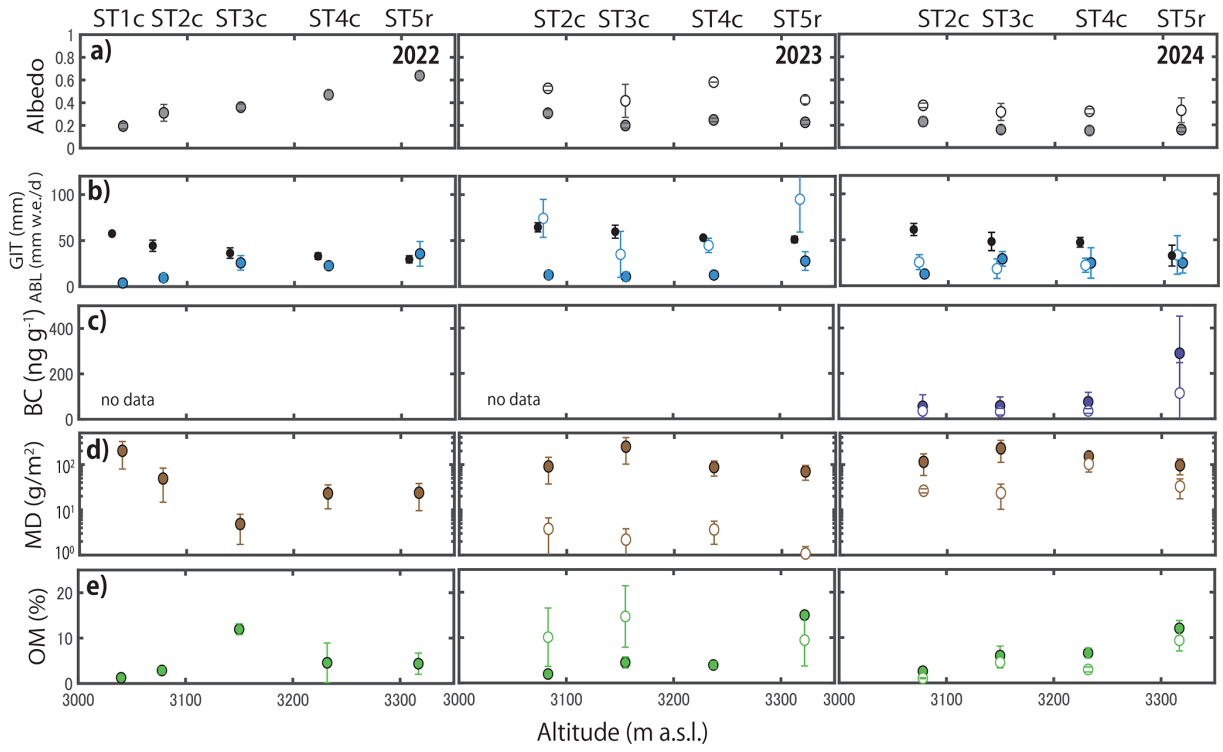


Figure 5. Altitudinal distribution of BB albedo **(a)**, granular ice thickness (GIT), ablation rate (ABL) **(b)**, black carbon (BC) **(c)**, mineral dust (MD) **(d)**, organic matter ratio (OM %) **(e)**. Open circle represents the clean area, while a filled circle indicates the dark area in 2023 and 2024. In panel **(b)**, black circles indicate ABL, and blue open circles and blue filled circles denote GIT in the clean and dark areas, respectively. The vertical axis of MD **(d)** is logarithmic. Vertical error bars indicate the standard deviations of each multiple measurement. In 2022, sampling was not conducted separately in dark and clean areas. For 2023 and 2024, filled circles represent data from dark surface areas, whereas open circles represent data from clean surface areas.

$75.7 \pm 5.3\,\mathrm{g\,m^{-2}}$ (range: 4.0–248.5 $\mathrm{g\,m^{-2}}$), and 6.5 % (range: 1.0 %–15.0 %), respectively. The BC concentration measured in 2024 was 86 $\mathrm{ng\,g^{-1}}$ (range: 31–289 $\mathrm{ng\,g^{-1}}$).

To ensure consistency with previous studies, only data obtained from ice surface samples were compared. The MD values were of the same order of magnitude as those reported for the Urumqi Glacier (200–500 $\mathrm{g\,m^{-2}}$) (8 %–12 % : OM %) (Takeuchi e al., 2008) and the Qiyi Glacier in the Qilian Mountains (30.4–873 $\mathrm{g\,m^{-2}}$) (7 %–11 % : OM %) (Takeuchi et al., 2005), whereas slightly lower values were observed in the Suntar-Khayata Mountain Range, Russian Siberia (0.1–43 $\mathrm{g\,m^{-2}}$) (Takeuchi et al., 2015).

Regarding BC, measurements conducted on the Tibetan Plateau using the thermal–optical method reported concentrations exceeding 3000 $\mathrm{ng\,g^{-1}}$ in granular ice (Li et al., 2017). Another study found a lower concentration of 369 $\mathrm{ng\,g^{-1}}$, likely influenced by outflow through meltwater (Zhang et al., 2020).

From the graphs of GIT and ABL presented in Fig. 5, it is evident that, when compared with the variations in ABL and GIT, the granular ice layers undergo melting within less than a day. This finding implies that the development and persistence of granular ice layers are highly transient and reflect the prevailing meteorological conditions on the corresponding day.

At ST2c, the OM % was consistently lower (2 %–2.5 %) than at the other stakes (4 %–14 %) in all observed samples. This is likely due to numerous outcrops and bands of melt-out MD near ST2, resulting in a high rate of MD exposure. The rate of biological proliferation appears insufficient to keep pace with the rapid exposure of MD, resulting in low OM %. Field observations also indicated that the surface particles at ST2c were not particularly dark and appeared to reflect the colour of the melt-out MD.

In Fig. S2, XRD spectra of MD at each stake are shown. But the diffraction angles of each peak are almost the same at all stakes. The identical XRD peak positions suggest that the MD share a common origin. In the glacier observations, the MD on the glacier surface at ST2c was considered to originate primarily from outcrops melting out of the glacier, whereas at the other stakes, it was thought to derive from rocks that had fallen onto the glacier from the upstream nunatak. However, the results indicated little difference between the mineral compositions in both cases.

In both 2023 and 2024, the dark areas showed similar patterns in granular ice thickness (GIT), mineral dust (MD), and

OM % at the sampled sites. In contrast, a pronounced difference was observed between 2023 and 2024 in the clean areas. MD increased substantially in the white areas (from 2–3 $g\,m^{-2}$ in 2023 to 20–30 $g\,m^{-2}$ in 2024), accompanied by a pronounced decrease in OM % (from 9 %–15 % in 2023 to 1 %–9 % in 2024). The thickness of the granular ice also decreased (from more than 35 mm in 2023 to less than 33 mm in 2024), and BB albedo values declined (from 0.5 in 2023 to 0.3 in 2024) in the clean area. It is likely that MD deposition occurred between the winter of 2023 and the spring of 2024, resulting in an increase in mineral content per unit area. This, in turn, may have caused a decrease in OM % due to insufficient biological growth keeping pace with the rapid increase in MD. Thus, while the clean areas exhibited substantial changes, the dark areas showed little to no variation. The granular ice thickness was slightly thicker in 2024 than in 2023, and both MD concentrations and OM proportions showed little change between years in the dark area. In the dark areas, MD concentrations were already on the order of 100 $g\,m^{-2}$ in 2023, so even with an additional deposition of approximately 10 $g\,m^{-2}$ in 2024, the order of magnitude remained unchanged. Therefore, it is likely that meteorological conditions in 2024 were generally more favourable for weathering crust (granular ice) development in these portions of the glacier. However, in the clean areas, the granular ice layer was less developed in 2024 compared to 2023. This reason is discussed in Sect. 3.6.1.

3.3 Spectral albedo of the granular ice and the underlying bubble-rich ice

Spectral albedos of the natural granular ice surface and the underlying bubble-rich ice (Fig. 4) surface were measured in dark and clean surface areas (Fig. 6). Physical properties of granular ice and LAP amount and concentrations in the layer are summarised in Table S1 in the Supplement. Although we did not measure LAPs beneath the granular ice at the location with observed spectral albedo, it was clear that their concentrations were lower than those in the surface granular ice layer. Ueda et al. (2026b) also reported that shallow ice cores taken at ST3c and ST2c indicated that surface granular ice contains much larger LAP, while underlying ice contains only a few LAP at the Potanin Glacier.

During the observation period, the weather conditions were fine, with cloud amount around 2/10. Spectral albedo of dark surface was lower than that of the clean surface in both the visible and near-infrared spectral regions. In both dark and clean surfaces, the albedo at the granular ice surface was lower than at the ice surface below the granular ice layer at $\lambda > 850$ nm. The reason is the presence of LAPs, mainly in the granular ice layer. At $\lambda < 850$ nm, the spectral albedo of the granular ice surface was higher for both dark and clean ice surfaces than for the underlying ice surface. This would be due to light scattering by the ice particles that compose the surface granular layer in the near-infrared, where LAPs have a weak effect on albedo (Wiscombe and Warren, 1980).

In the visible regions, the bubble-rich ice-surface albedo after removing the darker granular ice layer (blue curve in Fig. 6a) does not increase to the level of the clean granular ice layer (red curve in Fig. 6b). This may be because the albedo of the underlying bubble-rich ice (blue curve in Fig. 6a), measured after removing both surface granular ice and particles, still contains particles within the ice crust. It is therefore necessary, in future work, to collect and analyse the particles contained in the bubble-rich ice layer beneath the granular ice layer.

3.4 Humic and fulvic acids

Humic substances contained in surface granular ice were analysed, and the results are summarised in Table 2. The difference in total carbon content between the 2022 and 2023 samples is most likely due to differences in sampling location. Although the 2023 samples contained relatively low amounts of both humic and fulvic acids, the proportions of these fractions in total organic matter on a carbon basis were comparable to those typically observed in common soils. (humic acids: 5.9 %–34 %; fuluvic acids: 6.2 %–24 %) (Watanabe and Kuwatsuka, 1991), indicating that the particles on the Potanin Glacier are as humified as the soil. In both years, both the humic and fulvic acid contents tended to be larger in the finer grain size of 53 µm or less, which may reflect the larger surface area of the minerals.

Figure S3 shows the diagram indicating the degree of humification of humic acids, which increases from the lower left to the upper right. Using this diagram, humic acids have been classified into Types A, B, Rp, and P. Type A characterised by higher condensed aromatic structures, is detected from dark soils such as Andisols and Mollisols (Ikeya et al., 2013, 2019), while Type B, containing more aliphatic structures, is observed in brown forest soils such as Inceptisols (Ikeya et al., 2003). Type Rp (meaning rotten plants), the lowest class with regard to the degree of humification, is frequently detected in young soils such as alluvial soils, and Type P, which was initially observed in Podzols and is characterized by specific absorptions in UV-visible spectra derived from green pigment (Kumada et al., 1967; Ikeya et al., 2019. Humic acids in the particles of Potanin Glacier are classified as Type P. However, since A_{600}/C ranged from 1.4 to 2.1, their degree of humification was evaluated as low, corresponding to Type Rp. Low $\Delta\log(A_{400}/A_{600})$ could be attributed to a pigment, although it was not a green one typical of Type P humic acids (data not shown). Such humic acids may have accumulated due to slow decomposition of organic matter from plant or microbial origins with slow progression of humification. Low $\log(A_{400}/A_{600})$ could be attributed to a pigment, although it was not a green one typical of Type (data not shown). Chromophore of the green pigment, 4,9-dihydroxyperylene-3,10-quinone, is substituted

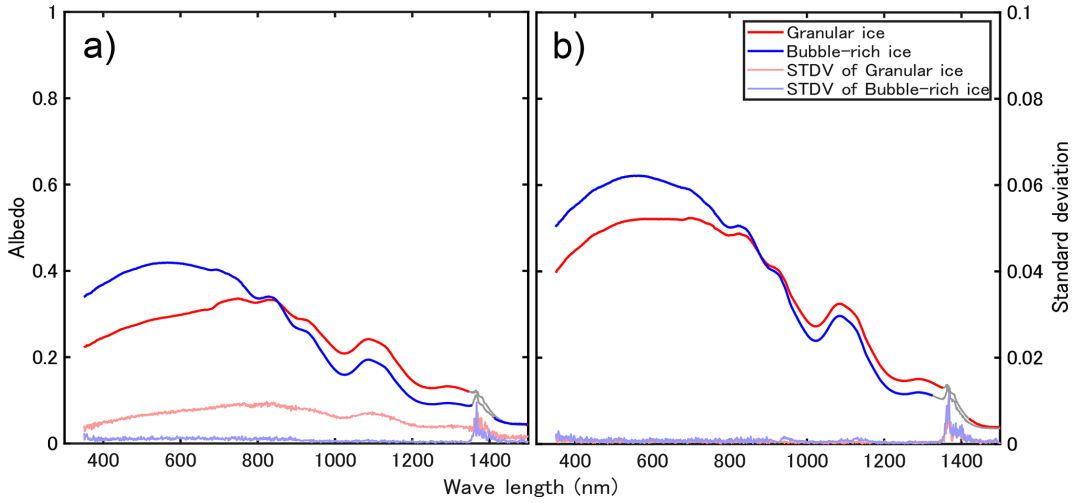


Figure 6. Spectral albedo observed on **(a)** dark and **(b)** clean surfaces at ST2c. Red lines indicate the spectral albedo at the surface of the granular ice. Blue lines indicate bubble-rich ice surface removed from surface granular ice. The standard deviations are plotted on the right y-axis using the corresponding light colors. Physical characteristics of granular ice and the amount of LAPs are summarised in Table S1.

Table 2. Results of analysis of humic substances in particles at the glacier surface.

Sampling	Particle size	Total carbon content	Humic acid content	Fulvic acid content	Degree of humification of humic acids	
year	µm	mg g^{-1}	%*	%*	$\Delta\log(A_{400}/A_{600})$	A_{600}/C
2022	< 53	26.7	16.2	7.7	0.647	1.57
2022	53–150	25.8	7.7	6.5	0.588	1.86
2023	< 53	9.2	3.9	4.1	0.630	1.40
2023	53–150	13.4	2.3	3.3	0.612	2.09

* Carbon basis.

with carboxy groups and/or hydroxyl groups and linked with aromatic or aliphatic moieties in humic acids and comprises the refractory fraction in humic acids (Ikeya et al., 2013). Although the pigment in the present humic acids is still unknown, it might also be enriched due to its recalcitrance.

3.5 Relation between LAP contents and Granular ice thickness to BB albedo

For each sample, BB albedo was measured five times, and the relationship between the BB albedo and the particle content per unit area is shown in Fig. 7. The average of uncertainty (standard deviation) of BB albedo was 0.019. The relation between BB albedo and each LAP (MD, OM and BC) indicates inverse correlation as in previous studies (Takeuchi et al., 2005; Yue et al., 2020). While, observed data showed that the greater the granular ice thickness (GIT), the higher the BB albedo based on observed data (Fig. 8). With increasing thickness of the granular ice layer, the scattering intensity of ice particles enhances, resulting in a further increase in albedo due to the dispersion of light-absorbing particles (LAPs) into the interstitial spaces or within the granular ice matrix on the surface of the weathering crust. We conclude that the effect of surface granular ice must be taken into account in the ice surface albedo, since the albedo of even these particle-rich mid-latitude glaciers changes significantly with the development of weathering crust. In other words, on ice albedo, it is necessary to consider not only albedo reduction due to LAPs, but also albedo increase due to granular ice layer development.

Some samples had low albedo ($\sim$0.1) even with thicker granular ice layer (2–5 mm), which indicates larger MD are included in granular ice layer in Fig. 8. The year-by-year relationships between LAPs, GIT, and BB albedo for 2022, 2023, and 2024 (Fig. S4) indicate that unlike in 2023 and 2024, the albedo in 2022 was primarily determined by the granular ice thickness, whereas in 2023 and 2024 it was mainly controlled by OM. Table 3 summarises the correlation coefficient between BB albedo and each LAP and WC thickness. All LAPs and GIT are logarithmic. Factors highly correlated with albedo varied widely from year to year, with WC thickness in 2022 and OM in 2023 and 2024. Overall, OM was the most highly correlated with BB albedo. The results indicate that in this glacier, OM predominantly deter-

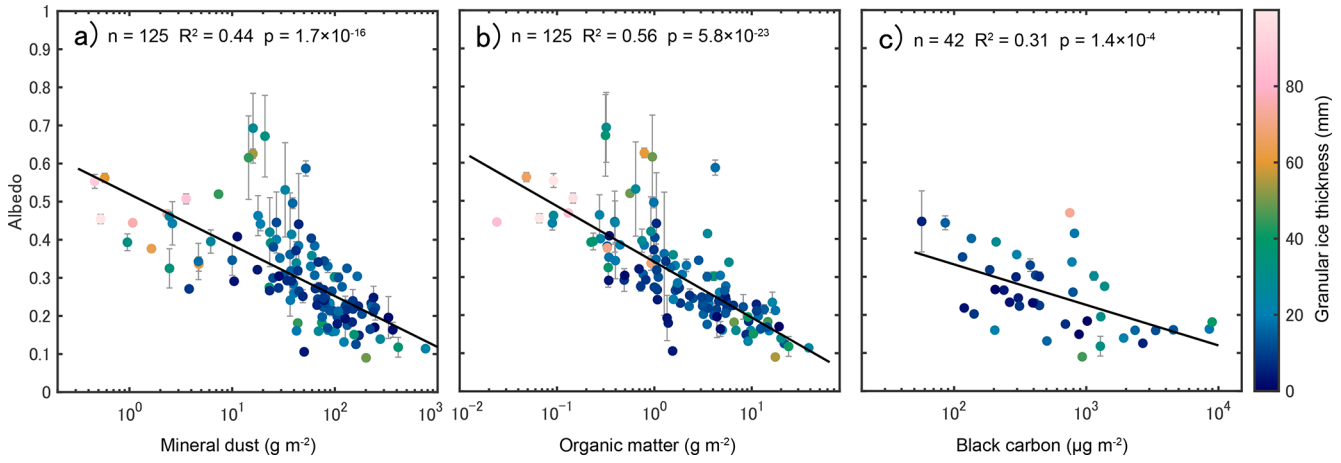


Figure 7. Relation between BB albedo and particles (MD, OM, BC) a)-c). The colour of the circle indicates surface granular ice thickness. All horizontal axes are logarithmic.

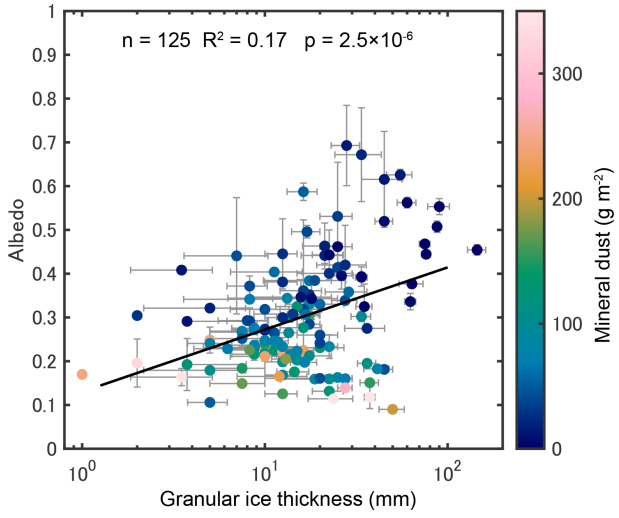


Figure 8. Relation between BB albedo and granular ice thickness (GIT). The circle colour indicates the amount of mineral dust per area.

mines albedo and further suggest that it contributes significantly to albedo reduction.

In previous research in Russian Siberia by Takeuchi et al. (2015), total particles on glaciers were not statistically significantly correlated with surface reflectivity ($\lambda = 0.350$–$1.050\,\mu m$), whereas algal biomass showed a significant negative correlation with surface reflectivity.

A multiple linear regression analysis was performed with BB albedo as the dependent variable and particle concentration and GIT as explanatory variables (Table 4). Multiple linear regression assumes that, with the other explanatory variables held constant, the relationship between the dependent variable and each explanatory variable is linear. In this study, the relationships between BB albedo and both particle concentration and GIT were non-linear; therefore, the explanatory variables were log-transformed to achieve linearization. Because $\log_{10}(X)$ is undefined when the particle concentration or GIT equals zero, the explanatory variables were transformed as $\log_{10}(X + A)$, where X denotes the particle concentration per unit area or GIT, and A is a constant set for each explanatory variable. The value of A was varied to maximise the absolute value of the correlation coefficient between $\log_{10}(X + A)$ and BB albedo. In terms of p-values, only GIT was statistically significant in 2022, GIT and OM were statistically significant in 2023, and only OM was statistically significant in 2024. MD was not statistically significant in any year. In addition, if MD acted as a light-absorbing particles, the t-value would be expected to be negative; however, it was positive in 2022. Overall, these results suggest that MD does not make a clear or consistent contribution to albedo reduction. Two possible explanations can be considered. First, mineral dust contains not only dark minerals but also relatively bright minerals such as quartz, which are expected to have a weaker effect on reducing albedo than other light-absorbing particles. Second, the surfaces of mineral particles may be coated with organic matter, such as humic substances, thereby masking the minerals' direct influence on albedo.

The most closely related explanatory variable to BB albedo was OM, followed by GIT, based on the t-values. The following equation is the result of a multiple regression analysis using the data from 2022 to 2024.

$$\begin{aligned}\mathrm{BBAlbedo} = {} & 0.2156 \times \log_{10}(\mathrm{GIT}\,[\mathrm{mm}] + 34) \\ & - 0.1446 \times \log_{10}\left(\mathrm{OM}\left[\mathrm{g\,m^{-2}}\right] + 0.06\right) \\ & - 0.0263 \end{aligned} \quad (1)$$

Table 3. Correlation coefficients (r) between BB albedo and each particle content or granular ice thickness. (GIT: granular ice thickness, OM: Organic matter, MD: Mineral dust, BC: Black carbon) The amounts of each particle and GIT are logarithmic. n, r, and p indicate the number of samples, the correlation coefficient, and the p-value, respectively.

year	n		log(GIT) (mm)	log(OM) ($\mathrm{g\,m^{-2}}$)	log(MD) ($\mathrm{g\,m^{-2}}$)	log(BC) ($\mu\mathrm{g\,m^{-2}}$)
2022	39	r	0.68	−0.43	−0.41	–
		p	1.7×10^{-6}	5.8×10^{-3}	9.8×10^{-3}	–
2023	44	r	0.68	−0.91	−0.85	–
		p	3.4×10^{-7}	3.3×10^{-17}	3.5×10^{-13}	–
2024	42*	r	0.11	−0.86	−0.76	−0.55
		p	0.48	3.6×10^{-13}	3.9×10^{-13}	1.4×10^{-4}
2022–2024	125	r	0.41	−0.75	−0.66	–
		p	2.4×10^{-6}	1.7×10^{-23}	3.7×10^{-17}	–

* The number of BC samples is 41.

Table 4. Summary of multiple regression analysis when the objective variable is BB albedo and the explanatory variables are GIT, MD, OM and BC. All explanatory variables are $\log_{10}$. R^2 denotes the coefficient of determination, and n indicates the number of samples. $A_{\mathrm{GIT}} = 34$, $A_{\mathrm{MD}} = 14$, $A_{\mathrm{OM}} = 0.06$, $A_{\mathrm{BC}} = 1.0$.

year	R^2 (n)		log(GIT + A_{GIT}) (mm)	log(MD + A_{MD}) ($\mathrm{g\,m^{-2}}$)	log(OM + A_{OM}) ($\mathrm{g\,m^{-2}}$)	log(BC + A_{BC}) ($\mu\mathrm{g\,m^{-2}}$)
2022	0.57 (39)	p	3.4×10^{-5}	0.65	0.22	–
		t	4.75	0.45	−1.24	–
2023	0.85 (44)	p	9.4×10^{-3}	0.59	2.9×10^{-7}	–
		t	2.73	−0.55	−6.15	–
2024	0.75 (42)	p	0.27	0.44	3.8×10^{-3}	0.50
		t	1.11	−0.77	− 3.09	−0.68
2022–2024	0.60 (125)	p	6.2×10^{-3}	0.23	1.2×10^{-7}	–
		t	2.8	−1.2	−5.6	–

Each GIT and OM has a limit on the available range as follows.

$5 \le \mathrm{GIT} \le 145(\mathrm{mm}), 0.024 \le \mathrm{OM} \le 23.92(\mathrm{g\,m^{-2}})$

BBalbedo was obtained using Eq. (1), and RMSE was 0.08. If both GIT and OM were zero, Eq. (1) predicts a BB albedo of 0.48. This value is 0.14 higher than the commonly reported albedo of clean ice (0.34) (Oerlmans and Knap, 1998). It represents the albedo of ice in the absence of both a granular layer and organic matter; however, the underlying ice beneath the granular layer contains abundant air bubbles (Fig. 4). Therefore, we infer that enhanced scattering by these bubbles leads to the higher albedo.

Based on the comparison of correlation coefficient values from simple correlation analysis (Table 3), as well as the absolute values of the t-statistics from multiple regression analysis (Table 4), it can be inferred that OM has a greater effect on albedo reduction than MD. Furthermore, the relationship between GIT and albedo, as indicated by both simple and multiple regression analyses, shows that GIT increases albedo.

3.6 Relation between LAPs and GIT

3.6.1 Relationships of GIT with MD and OM

Figure 9 illustrates the relationships between GIT and the concentrations of MD and OM within the granular ice layer. The concentrations were calculated by dividing the amount of particle per unit area by the granular ice thickness. The results show that higher concentrations of MD and OM lead to thinner GIT, indicating that the granular ice layer cannot grow thick when particle concentrations are high. The formation of weathering crust and the growth of a thick granular ice layer require the penetration of solar radiation into deeper layers. However, when high concentrations of particles are present at the surface, incoming solar radiation is absorbed by these particles in the uppermost layer. As a result, insuffi-

cient radiation reaches the deeper ice, thereby inhibiting the thickening of the granular ice layer. Aoki et al. (2011) also demonstrated that higher concentrations of surface particles reduce the amount of solar radiation transmitted to the underlying layer in a seasonal snowpack. Therefore, when modelling the development of weathering crust (granular ice) in future high-impurity Asian mountain glaciers, the key factor will be the solar radiation absorbed by light-absorbing substances.

Regarding the altitude profiles in 2023 and 2024, the MD and GIT values in the dark area were nearly the same, suggesting that the meteorological conditions were comparable (Fig. 5). However, in 2024, the MD concentration in the clean area increased by an order of magnitude, while the weathering crust became thinner. As indicated by the relationship described above, this is likely because an increase in particles on the glacier surface enhanced surface absorption of solar radiation, decreased transmitted radiation, and consequently led to thinning of the weathering crust.

3.6.2 Relationships among the three major light-absorbing particles

Here, we analyse the correlations among the various particles in Fig. 10. The concentration obtained by dividing by the GIT is the same as with Fig. 9. We can find a strong correlation between MD and OM (Fig. 10a), and a statistically significant relationship between OM and BC (Fig. 10b). Fig. 10c shows no statistical correlation between BC and MD. Several studies in Tibet have reported that BC, OC, and MD data obtained from snow and ice samples on glaciers are correlated (Zhang et al., 2020; Li et al., 2017), whereas no relationship was observed between BC and MD on the Potanin Glacier.

And also Yala Glacier in the Nepal Himalaya (Takeuchi et al., 2001), Urumqi No.1 Glacier (Takeuchi and Li, 2008), Qiyi Glacier in Qilian Mountain (Takeuchi et al., 2005)) and glaciers in Suntar-Khayata Mountain Range, Russian Siberia (Takeuchi et al., 2015) there have also been reports indicating that OM accounts for 4 %–12 % of the total particles, and that MD shows a strong correlation with OM. Similarly, a high correlation between OM and MD was observed on the Potanin Glacier in Mongolia.

The OM ratio ranged from 0.5 %–21.4 %, which was much wider than in previous studies.

Analyses of cryoconite granules that settle in small, water-filled circular holes on the ablation zones of glaciers and ice sheets have been extensively conducted. In Greenland, it has been reported that mineral particles serve as condensation nuclei, forming composite particles with organic matter, including extracellular polymeric substances (EPS) and decomposed materials, which are attached to their surfaces (Uetake et al., 2016). Langford et al. (2010) demonstrated that the interstices among mineral particles are filled with organic matter, including pigments and humic substances, and that the mineral particles are surrounded by humified organic matter. The glacier surface in the ablation zone exhibited characteristics similar to those of particles found within cryoconite holes. Takeuchi et al. (2015) and Chen et al. (2022) observed cryoconite granules on glacier surfaces composed of minerals and organic matter containing humic substances. In the glacier surface observed in this study, relatively large mineral particles were coated with organic matter, which are considered to function as condensation nuclei. Reports from the Greenland Ice Sheet indicate that MD on the glacier surface plays an important role as a nutrient for snow and ice microorganisms (McCutcheon et al., 2021). In Asian High Mountains regions, Nagatsuka et al. (2010) analysed the stable isotopic ratios of strontium (Sr), neodymium (Nd), and lead (Pb) in surface dust (cryoconite) by separating it into individual mineral and organic fractions, and demonstrated the potential transfer of nutrients from mineral to organic phases. Thus, since minerals are also important as nutrient sources for microorganisms, analyses from this perspective will be required in future research.

It was also found that OM shows a significant correlation with BC (Fig. 10b). These findings suggest that humic substances contain functional groups that likely retain and concentrate BC once it is deposited on OM. As a result of our analysis, we found that humic substances (humic acid and fulvic acid) are present in the OM (Sect. 3.5). Humic substances generally possess a variety of functional groups (such as carboxyl and phenolic groups) within their molecular structure, giving them adsorptive properties (Anesio et al., 2017; Antony et al., 2025). Previous studies have also reported the presence of cyanobacteria in the ablation zones of other glaciers. Therefore, it is possible that exopolysaccharides (EPS) secreted by cyanobacteria may be forming biofilms in Potanin Glacier as well. Thus, the adsorptive properties of humic substances and EPS could contribute to the aggregation and deposition of BC. However, microbial identification analysis was not performed in this study. These findings indicate that, in addition to albedo reduction caused by microorganisms and humic-derived organic matter, the adhesive nature of humic substances promotes the enrichment of BC within glacier surface particles, thereby providing a structure that can further decrease glacier albedo.

Based on the strength of correlations among LAPs and the properties of each particle, the relationships among LAPs can be conceptualised as follows: as illustrated in Fig. 11, MD produced by outcrops and weathering serve as the initial substrates. These MDs are thought to serve as aggregation nuclei for organic matter, with microorganisms and humic substances surrounding their surfaces. Through the presence of functional groups in humic substances and the formation of biofilms by EPS, BC becomes concentrated in OM–rich areas. Based on the above scenario, we can hypothesise the process of albedo reduction.

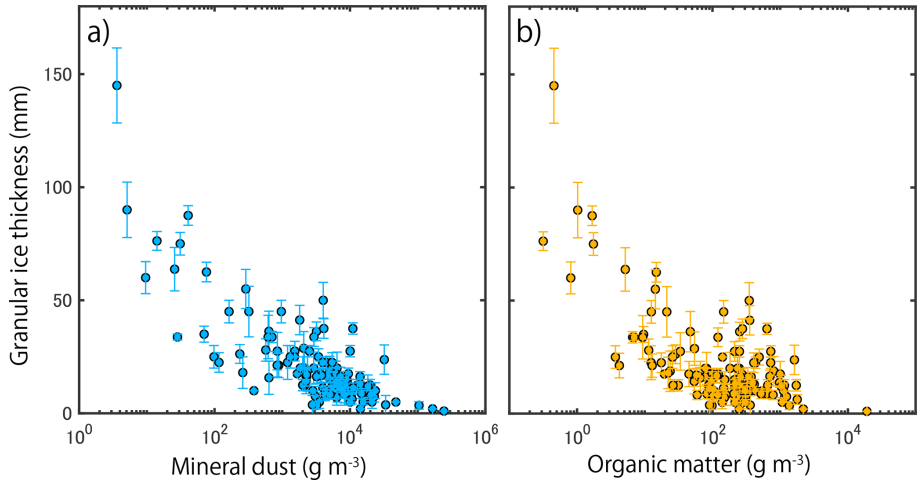


Figure 9. Relation between granular ice thickness and mineral dust concentration **(a)** and organic matter concentration **(b)**.

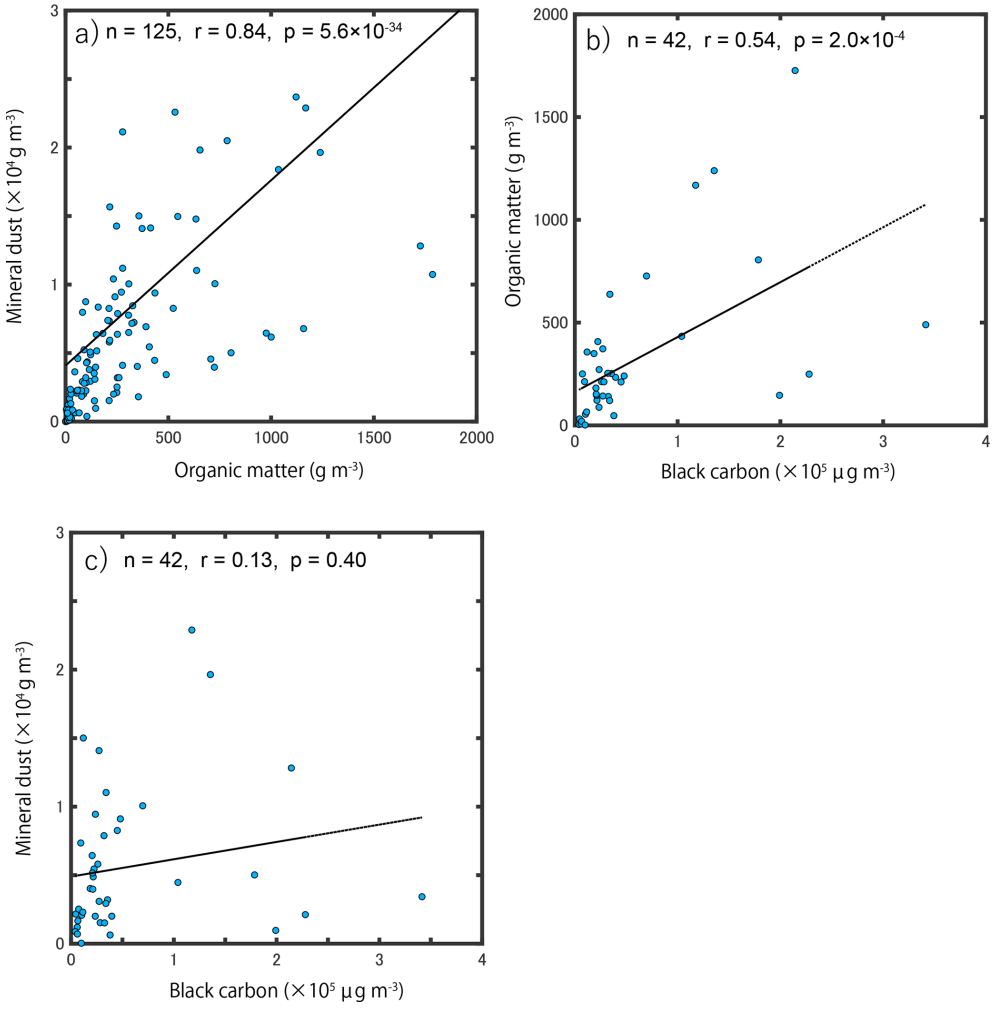


Figure 10. Relationships among the concentrations of the three major light-absorbing particles on the glacier surface: **(a)** mineral particles and organic matter; **(b)** black carbon and organic matter; **(c)** black carbon and mineral particles. Note that black carbon was sampled only in 2024, so there are only 42 samples.

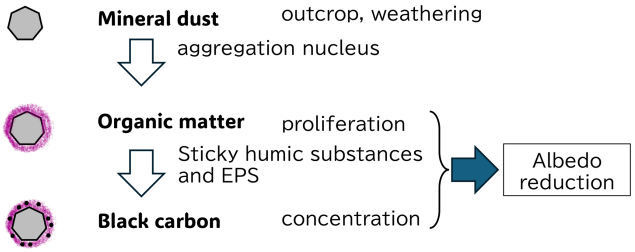


Figure 11. Schematic diagram showing the relationship between the three major LAPs (MD, OM, BC).

3.6.3 Limitations and future study

In this study, inverse correlations between broadband albedo and each LAP indicated that LAPs contributed to a reduction in albedo. However, to quantitatively compare the extent to which each LAP contributes to albedo reduction, future work should develop a radiative transfer model representing the observed weathering crust, composed of a granular ice layer containing abundant surface LAPs and an underlying bubble-rich ice layer. For this purpose, it is also necessary to determine the mass absorption coefficient of each LAP.

Regarding BC, the SP2 measures particles in the 70–3000 nm size range, which is considered to capture the majority of the BC mass. Nevertheless, BC particles strongly adhered to coarse mineral grains may have been underestimated due to limitations in the SP2 measurement system's transmission efficiency. Therefore, the sampling procedure needs to be improved so that, in future studies, all BC contained in particles on the glacier surface can be quantified. As a possible solution, BC in particle samples can be measured using the thermal–optical method; however, for the Potanin Glacier particle samples, the concentrations of MD and OM were too high to allow BC quantification by the thermal–optical method.

In this study, the sources of individual particles were not analysed. These particles may originate from atmospheric deposition or exposure of englacial materials, while for organic matter, in situ microbial growth on the glacier surface should also be considered. To better understand the processes governing albedo variations on glaciers, future studies should evaluate the surface mass balance of each particle, including the portion removed by meltwater flow and examine the relationships between particle variability, meteorological conditions, and the evolution of the weathering crust layer.

4 Conclusions

Field observations of shallow ice cores and ice temperature revealed that the weathering crust layer in the ablation zone of Potanin Glacier can be divided into a surface granular ice layer and an underlying bubble-rich ice layer. Our observations of broadband (BB) albedo, granular ice thickness (GIT), and light-absorbing particle (LAP: mineral dust (MD), organic matter (OM), black carbon (BC)) concentrations indicate that glacier surface albedo is inversely correlated with OM content among the particles, consistent with prior studies. Additionally, a positive correlation between BB albedo and granular ice thickness was identified. The correlation coefficients between BB albedo and GIT, MD, and OM varied annually, and in some years, no significant correlation was observed between albedo and either GIT or MD. However, across all years, the negative correlation between albedo and OM remained significant. Furthermore, multiple regression analysis of data from 2022–2024 revealed that albedo is strongly related to both GIT and OM, allowing broadband albedo to be robustly estimated by a regression model incorporating these two variables.

Analysis of humic substances among the particles showed that the combined proportion of humic acid and fulvic acid relative to total carbon ranged from 2.3 % to 16.2 %, demonstrating evidence of soil formation on the glacier surface. Correlation analysis among light-absorbing particles further suggests MD act as aggregation nuclei for organic matter, with their surfaces supporting microbial adhesion and humic substance accumulation, which in turn facilitate the capture and enrichment of BC on the glacier surface.

Measurements of the granular ice thickness indicated that it is typically less than the daily ablation rate, suggesting that the granular ice layer melts completely within a single day and is subsequently renewed from the underlying weathering crust. This process is notably influenced by impurity concentrations: when particles are abundant, granular ice layers do not thicken appreciably. Going forward, detailed observations of the attenuation coefficient attributable to particles within granular ice will be crucial for advancing models of granular ice layer evolution on glaciers.

Data availability. Data used in this paper is saved on Zenodo https://doi.org/10.5281/zenodo.18437674 (Sakai, 2026).

Supplement. The supplement related to this article is available online at https://doi.org/10.5194/tc-20-5181-2026-supplement.

Author contributions. Structure of the study: AS, NT, TT, TA, KO. Observation and Sample collection: AS, KP, SM, MO, KK. Sample analysis: AS, KK, MO, SU, SO, AW, KO, NT, SM. Writing (original draft preparation): AS. Funding acquisition: AS, NT, SO, TA. Writing (review and editing): all authors.

Competing interests. The contact author has declared that none of the authors has any competing interests.

Disclaimer. Publisher's note: Copernicus Publications remains neutral with regard to jurisdictional claims made in the text, published maps, institutional affiliations, or any other geographical representation in this paper. The authors bear the ultimate responsibility for providing appropriate place names. Views expressed in the text are those of the authors and do not necessarily reflect the views of the publisher.

Acknowledgements. We would like to thank Dr. Noboru Furukawa of Chiba University for helping with XRD analysis. We also thank S. Sunako, N. Ishida, K. Yasue, S. Ogawa, Y. Kurosaki, K. Kondo, S. Nishino and M. Kito for their support during the field observations. We are grateful to T. Ozat, B. Bulganbaatar, N. Yura, B. Syerjuma, Z. Erkebek, O. Nurbol at the Center for Hydrology, Meteorology and Environment Monitoring of Bayan Ulgii for their invaluable assistance and support during our fieldwork at Potanin Glacier. We thank S. McKenzie Skiles and anonymous reviewers for their valuable comments and constructive reviews.

Financial support. This research has been supported by the JSPS-KAKENHI (20H00196 and 25H00507) and the Transnational Doctoral Program for Leading Professional in Asian Countries at Nagoya University.

Review statement. This paper was edited by S. McKenzie Skiles and reviewed by two anonymous referees.

References

Anesio, A. M., Lutz, S., Chrismas, N. A. M., and Bennning, L. G.: The microbiome of glaciers and ice sheets, npj Biofilms Microbiomes, 3, 10, https://doi.org/10.1038/s41522-017-0019-0, 2017.

Antony, R., Rossel, P. E., Feord, H. K., Dittmar, T., Tranter, M., Anesio, A. M., and Benning, L. G.: Extraction strategies for profiling the molecular composition of particulate organic matter on glacier surfaces, Environ. Sci. Technol., 59, 4455–4468, https://doi.org/10.1021/acs.est.4c10088, 2025.

Aoki, T., Fukabori, M., Hachikubo, A., Tachibana, Y., and Nishio, F.: Effects of snow physical parameters on spectral albedo and bidirectional reflectance of snow surface, J. Geophys. Res., 105, 10219– 10236, https://doi.org/10.1029/1999JD901122, 2000.

Aoki, T., Hachikubo, A., and Hori, M.: Effects of snow physical parameters on shortwave broadband albedos, J. Geophys. Res., 108, 4616, https://doi.org/10.1029/2003JD003506, 2003.

Aoki, T., Kuchiki, K., Niwano, M., Kodama, Y., Hosaka, M., and Tanaka, T.: Physically based snow albedo model for calculating broadband albedos and the solar heating profile in snowpack for general circulation models, J. Geophys. Res., 116, D11114, https://doi.org/10.1029/2010JD015507, 2011.

Braithwaite, R. J.: Positive degree-day factors for ablation on the Greenland ice sheet studied by energy-balance modelling, J. Glaciol., 41, 153–160, https://doi.org/10.3189/S0022143000017846, 1995.

Chen, Y., Takeuchi, N., Wang, F., and Li, Z.: Characteristics of chemical solutes and mineral dust in ice of the ablation area of a glacier in the Tien Shan Mountains, Central Asia, Front. Earth Sci., 10, 904261, https://doi.org/10.3389/feart.2022.904261, 2022.

Christner, B. C., Lavender, H. F., Davis, C. L., Oliver, E. E., Neuhaus, S. U., Myers, K. F., Hagedorn, B., Tulaczyk, S. M., Doran, P. T., and Stone, W. C.: Microbial processes in the weathering crust aquifer of a temperate glacier, The Cryosphere, 12, 3653–3669, https://doi.org/10.5194/tc-12-3653-2018, 2018.

Cook, J. M., Hodson, A. J., and Irvine-Fynn, T. D. L.: Supraglacial weathering crust dynamics inferred from cryoconite hole hydrology, Hydrol. Process., 30, 433–446, https://doi.org/10.1002/hyp.10602, 2016.

Cook, J. M., Hodson, A. J., Gardner, A. S., Flanner, M., Tedstone, A. J., Williamson, C., Irvine-Fynn, T. D. L., Nilsson, J., Bryant, R., and Tranter, M.: Quantifying bioalbedo: a new physically based model and discussion of empirical methods for characterising biological influence on ice and snow albedo, The Cryosphere, 11, 2611–2632, https://doi.org/10.5194/tc-11-2611-2017, 2017a.

Cook, J. M., Hodson, A. J., Taggart, A. J., Mernild, S. H., and Tranter, M.: A predictive model for the spectral "bioalbedo" of snow, J. Geophys. Res.-Earth, 122, 434–454, https://doi.org/10.1002/2016JF003932, 2017b.

Cooper, M. G., Smith, L. C., Rennermalm, A. K., Miège, C., Pitcher, L. H., Ryan, J. C., Yang, K., and Cooley, S. W.: Meltwater storage in low-density near-surface bare ice in the Greenland ice sheet ablation zone, The Cryosphere, 12, 955–970, https://doi.org/10.5194/tc-12-955-2018, 2018.

Dean, W. E.: Determination of carbonate and organic matter in calcareous sediments and sedimentary rocks by loss on ignition; comparison with other methods, J. Sediment. Res., 44, 242–248, 1974.

Di Mauro, B. and Fugazza, D.: Pan-Alpine glacier phenology reveals lowering albedo and increase in ablation season length, Remote Sens. Environ., 279, 113119, https://doi.org/10.1016/j.rse.2022.113119, 2022.

Dumont, M., Arnaud, L., Picard, G., Libois, Q., Lejeune, Y., Nabat, P., Voisin, D., and Morin, S.: In situ continuous visible and near-infrared spectroscopy of an alpine snowpack, The Cryosphere, 11, 1091–1110, https://doi.org/10.5194/tc-11-1091-2017, 2017.

Flanner, M. G. and Zender, C. S.: Linking snowpack microphysics and albedo evolution, J. Geophys. Res., 111, D12208, https://doi.org/10.1029/2005JD006834, 2006.

Flanner, M. G., Arnheim, J. B., Cook, J. M., Dang, C., He, C., Huang, X., Singh, D., Skiles, S. M., Whicker, C. A., and Zender, C. S.: SNICAR-ADv3: a community tool for modeling spectral snow albedo, Geosci. Model Dev., 14, 7673–7704, https://doi.org/10.5194/gmd-14-7673-2021, 2021.

Flanner, M. G., Zender, C. S., Randerson, J. T., and Rasch, P. J.: Present-day climate forcing and response from black carbon in snow, J. Geophys. Res., 112, D11202, https://doi.org/10.1029/2006JD008003, 2007.

Greuell, W. and Smeets, P.: Variations with elevation in the surface energy balance on the Pasterze (Austria), J. Geophys. Res., 106, 31717–31727, 2001.

Halbach, L., Chevrollier, L. A., Doting, E. L., Fahrner, S., Langford, H., McCutcheon, J., Pearce, D. A., Rassner, S. M. E., and Edwards, A.: Pigment signatures of algal communities and their implications for glacier surface darkening, Sci. Rep., 12, 17643, https://doi.org/10.1038/s41598-022-22271-4, 2022.

Hartl, L., Felbauer, L., Schwaizer, G., and Fischer, A.: Small-scale spatial variability in bare-ice reflectance at Jamtalferner, Austria, The Cryosphere, 14, 4063–4081, https://doi.org/10.5194/tc-14-4063-2020, 2020.

Hugonnet, R., McNabb, R., Berthier, E., Menounos, B., Nuth, C., Girod, L., Farinotti, D., Huss, M., Dussaillant, I., Brun, F., and Kääb, A.: Accelerated global glacier mass loss in the early twenty-first century, Nature, 592, 726–731, https://doi.org/10.1038/s41586-021-03436-z, 2021.

Ikeya, K. and Watanabe, A.: Direct expression of an index for the degree of humification of humic acids using organic carbon concentration, Soil Sci. Plant Nutr., 49, 47–53, https://doi.org/10.1080/00380768.2003.10409978, 2003.

Ikeya, K., Sleighter, R. L., Hatcher, P. G., and Watanabe, A.: Fourier transform ion cyclotron resonance mass spectrometric analysis of the green fraction of soil humic acids, Rapid. Commun. Mass Sp., 27, 2559–2568, https://doi.org/10.1002/rcm.6718, 2013.

Ikeya, K., Maie, N., Han, X., Wang, G., and Watanabe, A.: Comparison of carbon skeletal structures in black humic acids from different soil origins, Soil Sci. Plant Nutr., 65, 109–113, https://doi.org/10.1080/00380768.2019.1584016, 2019.

Irvine-Fynn, T. D., Cook, J. M., Edwards, A., Mowlem, M. C., Hodson, A. J., and Tranter, M.: Storage and export of microbial biomass across the western Greenland ice sheet, Nat. Commun., 12, 3960, https://doi.org/10.1038/s41467-021-24040-9, 2021.

Khalzan, P., Sakai, A., and Fujita, K.: Mass balance of four Mongolian glaciers: In-situ measurements, long-term reconstruction and sensitivity analysis, Front. Earth Sci., 9, 785306, https://doi.org/10.3389/feart.2021.785306, 2022.

Khalzan, P., Sadyrov, S., Sakai, A., Tanaka, K., and Fujita, K.: Glacier meltwater contribution to river runoff in Western Mongolia, J. Hydrol.-Regional Studies, 59, 102375, https://doi.org/10.1016/j.ejrh.2025.102375, 2025.

Kumada, K., Watanabe, A., Uchida, Y., and Saigusa, M.: Studies on the humus composition of Japanese soils, Soil Sci. Plant Nutr., 13, 1–8, 1967.

Kuwatsuka, S., Watanabe, A., Itoh, K., and Arai, S.: Comparison of two methods of preparation of humic and fulvic acids, IHSS method and NAGOYA method, Soil Sci. Plant Nutr., 38, 23–30, https://doi.org/10.1080/00380768.1992.10416948, 1992.

Langford, H., Hodson, A., Banwart, S., and Bøggild, C.: The microstructure and biogeochemistry of Arctic cryoconite granules, Ann. Glaciol., 51, 87–94, https://doi.org/10.3189/172756411795932083, 2010.

Leifeld, J.: Thermal stability of black carbon characterised by oxidative differential scanning calorimetry, Org. Geochem., 38, 112–127, https://doi.org/10.1016/j.orggeochem.2006.08.004, 2007.

Li, X., Kang, S., He, X., Qu, B., Tripathee, L., Jing, Z., Paudyal, R., Li, Y., Zhang, Y., Yan, F., Li, G., and Li, C.: Light-absorbing impurities accelerate glacier melt in the central Tibetan Plateau, Sci. Total Environ., 587–588, 310–319, 2017.

McCutcheon, J., Lutz, S., Williamson, C., Cook, J. M., Tedstone, A. J., Vanderstraeten, A., Wilson, S. A., Stockdale, A., Bonneville, S., McQuaid, J. B., Tranter, M., Hawkings, J., Wadham, J., and Irvine-Fynn, T.: Mineral phosphorus drives glacier algal blooms on the Greenland Ice Sheet, Nat. Commun., 12, 570, https://doi.org/10.1038/s41467-020-20627-w, 2021.

Mori, T., Moteki, N., Ohata, S., Koike, M., Goto-Azuma, K., Miyazaki, Y., and Kondo, Y.: Improved technique for measuring the size distribution of black carbon particles in liquid water, Aerosol Sci. Tech., 50, 242–254, https://doi.org/10.1080/02786826.2016.1147644, 2016.

Moteki, N., Kondo, Y., and Nakamura, S.: Method to measure refractive indices of small nonspherical particles: application to black carbon particles, J. Aerosol Sci., 41, 513–521, https://doi.org/10.1016/j.jaerosci.2010.02.013, 2010.

Naegeli, K. and Huss, M.: Sensitivity of mountain glacier mass balance to changes in bare-ice albedo, Ann. Glaciol., 58, 119–129, https://doi.org/10.1017/aog.2017.25, 2017.

Nagatsuka, N., Takeuchi, N., Nakano, T., Kokado, E., and Li, Z.: Sr, Nd and Pb stable isotopes of surface dust on Ürümqi glacier No. 1 in western China, Ann. Glaciol., 51, 95–105, https://doi.org/10.3189/172756411795931895, 2010.

Nagatsuka, N., Takeuchi, N., Uetake, J., Shimada, R.: Mineralogical composition of cryoconite on glaciers in northwest Greenland, Bull. Glaciol. Res., 32, 107–114, https://doi.org/10.5331/bgr.32.107, 2014.

Onuma, Y., Takeuchi, N., Tanaka, S., Nagatsuka, N., Niwano, M., and Aoki, T.: Physically based model of the contribution of red snow algal cells to temporal changes in albedo in northwest Greenland, The Cryosphere, 14, 2087–2101, https://doi.org/10.5194/tc-14-2087-2020, 2020.

Oerlemans, J. and Knap, W. H.: A 1 year record of global radiation and albedo in the ablation zone of Morteratschgletscher, Switzerland, J. Glaciol., 44, 231–238, https://doi.org/10.3189/S0022143000002574, 1998.

Painter, T. H., Duval, B., and Thomas, W. H.: Detection and quantification of snow algae with an airborne imaging spectrometer, Appl. Environ. Microb., 67, 5267–5272, https://doi.org/10.1128/AEM.67.11.5267-5272.2001, 2001.

Pan, C. G., Pope, A., Kamp, U., Dashtseren, A., Walther, M., and Syromyatina, M. V.: Glacier recession in the Altai Mountains of Mongolia in 1990–2016, Geogr. Ann. A, 100, 1–19, https://doi.org/10.1080/04353676.2017.1407560, 2017.

Pan, C. G., Kamp, U., Munkhjargal, M., Halvorson, S. J., Dashtseren, A., and Walther, M.: An estimated contribution of glacier runoff to Mongolia's Upper Khovd River Basin in the Altai Mountains, Mt. Res. Dev., 39, 12–20, https://doi.org/10.1659/MRD-JOURNAL-D-18-00059.1, 2019.

Pellicciotti, F., Brock, B., Strasser, U., Burlando, P., Funk, M., and Corripio, J.: An enhanced temperature-index glacier melt model including the shortwave radiation balance: development and testing for Haut Glacier d'Arolla, Switzerland, J. Glaciol., 51, 573–587, https://doi.org/10.3189/172756505781829124, 2005.

Picard, G. and Libois, Q.: Simulation of snow albedo and solar irradiance profile with the Two-streAm Radiative TransfEr in Snow (TARTES) v2.0 model, Geosci. Model Dev., 17, 8927–8953, https://doi.org/10.5194/gmd-17-8927-2024, 2024.

Sakai, A.: Ice albedo and its relationship with light-absorbing impurities and weathering crust at the Potanin Glacier, Mongolia, Zenodo [data set], https://doi.org/10.5281/zenodo.18437674, 2026.

Sinha, P. R., Kondo, Y., Goto-Azuma, K., Tsukagawa, Y., Fukuda, K., Koike, M., Mori, T., Oshima, N., Førland, E. J., Irwin, M., Gallet, J.-C., and Pedersen, C. A.: Seasonal progression of the deposition of black carbon by snowfall at Ny-

Ålesund, Spitsbergen, J. Geophys. Res.-Atmos., 123, 997–1016, https://doi.org/10.1002/2017JD028027, 2018.

Skiles, S. M. and Painter, T. H.: Daily evolution in dust and black carbon content, snow grain size, and snow albedo during snowmelt, Rocky Mountains, Colorado, J. Glaciol., 63, 118–132, https://doi.org/10.1017/jog.2016.125, 2017.

Takeuchi, N. and Li, Z.: Characteristics of surface dust on Ürümqi Glacier No. 1 in the Tien Shan Mountains, China, Arct. Antarct. Alp. Res., 40, 744–750, https://doi.org/10.1657/1523-0430(07-094)[TAKEUCHI]2.0.CO;2, 2008.

Takeuchi, N., Kohshima, S., and Seko, K.: Structure, formation, and darkening process of albedo reducing material (cryoconite) on a Himalayan glacier: a granular algal mat growing on the glacier, Arct. Antarct. Alp. Res., 33, 115–122, https://doi.org/10.2307/1552211, 2001.

Takeuchi, N., Matsuda, Y., Sakai, A., and Fujita, K.: A large amount of biogenic surface dust (cryoconite) on a glacier in the Qilian Mountains, China, Bull. Glaciol. Res., 22, 1–8, 2005.

Takeuchi, N., Fujisawa, Y., Kadota, T., Tanaka, S., Miyairi, M., Shirakawa, T., Kusaka, R., Fedorov, A. N., Konstantinov, P., and Ohata, T.: The effect of impurities on the surface melt of a glacier in the Suntar-Khayata mountain range, Russian Siberia, Front. Earth Sci., 3, 82, https://doi.org/10.3389/feart.2015.00082, 2015.

Tedstone, A. J., Cook, J. M., Williamson, C. J., Hofer, S., McCutcheon, J., Irvine-Fynn, T., Gribbin, T., and Tranter, M.: Algal growth and weathering crust state drive variability in western Greenland Ice Sheet ice albedo, The Cryosphere, 14, 521–538, https://doi.org/10.5194/tc-14-521-2020, 2020.

The GlaMBIE Team: Community estimate of global glacier mass changes from 2000 to 2023, Nature, 639, 382–388, https://doi.org/10.1038/s41586-024-08545-z, 2025.

Traversa, G. and Di Mauro, B.: Weathering crust formation outpaces melt-albedo feedback on blue ice shelves of East Antarctica, Commun. Earth Environ., 5, 740, https://doi.org/10.1038/s43247-024-01896-5, 2024.

Ueda, S., Ohata, S., Iizuka, Y., Seki, O., Matoba, S., Matsui, H., Koike, M., and Kondo, Y.: Evaluation of sample storage methods for single particle analyses of black carbon in snow and ice: Merits and risks of glass and plastic vials for melted sample storage, Aerosol Sci. Tech., 60, 5–20, https://doi.org/10.1080/02786826.2025.2542900, 2026a.

Ueda, S., Sakai, A., Ohata, S., Khalzan, P., Matoba, S., Kondo, K., and Matsui, H.: Concentration and size distribution of black carbon over the ablation area of Potanin glacier: enrichment ability of surface weathering granular ice of water-insoluble particles with snow/ice melting, Atmos. Chem. Phys., 26, 3167–3184,https://doi.org/10.5194/acp-26-3167-2026, 2026b.

Uetake, J., Tanaka, S., Segawa, T., Takeuchi, N., Nagatsuka, N., Motoyama, H., and Aoki, T.: Microbial community variation in cryoconite granules on Qaanaaq Glacier, NW Greenland, FEMS Microbiol. Ecol., 92, fiw127, https://doi.org/10.1093/femsec/fiw127, 2016.

Watanabe, A. and Kuwatsuka, S.: Triangular diagram for humus composition in various types of soils, Soil Sci. Plant Nutr., 49, 167–170, 1991.

Watanabe, A., Kawasaki, S., Kitamura, S., and Yoshida, S.: Temporal changes in humic acids in cultivated soils with continuous manure application, Soil Sci. Plant Nutr., 53, 535–544, https://doi.org/10.1111/j.1747-0765.2007.00170.x, 2007.

Warren, S. G.: Optical properties of snow, Rev. Geophys., 20, 67–89, https://doi.org/10.1029/RG020i001p00067, 1982.

Warren, S. G. and Wiscombe, W. J.: A model for the spectral albedo of snow. II: Snow containing atmospheric aerosols, J. Atmos. Sci., 37, 2734–2745, 1980.

Whicker, C. A., Flanner, M. G., Dang, C., Zender, C. S., Cook, J. M., and Gardner, A. S.: SNICAR-ADv4: a physically based radiative transfer model to represent the spectral albedo of glacier ice, The Cryosphere, 16, 1197–1220, https://doi.org/10.5194/tc-16-1197-2022, 2022.

Woods, T. and Hewitt, I. J.: A model of the weathering crust and microbial activity on an ice-sheet surface, The Cryosphere, 17, 1967–1987, https://doi.org/10.5194/tc-17-1967-2023, 2023.

Yue, X., Li, Z., Zhao, J., Fan, J., Takeuchi, N., and Wang, L.: Variation in albedo and its relationship with surface dust at Urumqi Glacier No. 1 in Tien Shan, China, Front. Earth Sci., 8, 110, https://doi.org/10.3389/feart.2020.00110, 2020.

Zhang, Y., Gao, T., Kang, S., Sprenger, M., Tao, S., Du, W., Yang, J., Wang, F., and Meng, W.: Effects of black carbon and mineral dust on glacial melting on the Muz Taw glacier, Central Asia, Sci. Total Environ., 740, 140056, https://doi.org/10.1016/j.scitotenv.2020.140056, 2020.

Zhang, Y., Kang, S., Cong, Z., Schmale, J., Sprenger, M., Li, C., Yang, W., Gao, T., Sillanpää, M., Li, X., Liu, Y., Chen, P., and Zhang, X.: Light-absorbing impurities enhance glacier albedo reduction in the southeastern Tibetan plateau, J. Geophys. Res.-Atmos., 122, 6915–6933, https://doi.org/10.1002/2016JD026397, 2017.